The Effect of Rotation and Surface Friction on Orographic Drag

HARALDUR ÓLAFSSON AND PHILIPPE BOUGEAULT

Météo-France, Centre National de Recherches Météorologiques, Toulouse, France

(Manuscript received 22 December 1995, in final form 27 June 1996)

ABSTRACT

A numerical, hydrostatic model is used to investigate the form and magnitude of the pressure drag created by 3D elliptical mountains of various heights (h) and aspect ratios (R) in flows characterized by uniform upstream velocity (U) and stability (N). Three series of simulations, corresponding to increasing degrees of realism, are performed: (i) without rotation and surface friction; (ii) with rotation, but no surface friction; (iii) with rotation and surface friction. For the simulations with rotation, the Coriolis parameter has a typical midlatitude value and the upstream flow is geostrophically balanced. The surface friction is introduced by the use of a typical roughness length.

For low values of the nondimensional height (Nh/U), the pressure drag is reduced by the effect of rotation, in agreement with well-known results of linear theory. This seems to be valid until $Nh/U \sim 1.4$, that is, in the high drag regime. On the other hand, for large values of Nh/U, that is, in the blocked flow regime, rotation has the opposite effect and increases the drag. The authors propose a simple interpretation of these results: that geostrophic adjustment acts to first order as a relaxation toward the upstream velocity. For low Nh/U, the acceleration above the mountain is a dominating feature of the flow and here the flow is slowed by the presence of rotation. For high Nh/U, when upstream blocking is dominant, the flow is slowed by the mountain and therefore accelerated by rotation. For values of $Nh/U \sim 1.4$, the rotation is sufficient to force a transition from the blocked state to the unblocked state. The influence of rotation may therefore extend the range of usefulness of linear theory.

Surface friction dramatically suppresses wave breaking at all values of Nh/U. The induced effect on the drag is negligible for $Nh/U > 3$, but there is a strong reduction at smaller values of Nh/U. In fact, the high-drag regime is nearly suppressed.

The overall combined effect of rotation and surface friction is to constrain the drag (and to some extent, the flow patterns) to values remarkably close to the linear prediction. This sheds some light on recent, but as yet unexplained, results from the PYREX field experiment. The authors conclude this paper by running a real case drawn from this experiment, which reveals a behavior consistent with the idealized scenarios.

1. Introduction

Orographic drag is recognized to be an important sink of atmospheric momentum (e.g. Eliassen and Palm 1960; Lilly 1972; Wahr and Oort 1984), and knowledge of its behavior is therefore essential in studies of the large-scale momentum budget.

Scaling of the equations that govern frictionless, hydrostatic, Boussinesq flow on a nonrotating plane (e.g., Smith and Grønås 1993) shows that the governing parameters for orographic flow are the obstacle shape and aspect ratio, together with Nh/U, where N is the Brunt–Väisälä frequency, h is obstacle (mountain) height, and U is the upstream wind. Here, Nh/U is often referred to as the nondimensional mountain height (or the inverse Froude number). This number can be regarded as a measure of the importance of the nonlinear terms in the equations of motion. In a 3D flow with high Nh/U, the kinetic energy is not sufficient for the flow to overcome the potential barrier of the obstacle and the flow must split. In flow on a rotating plane (hereafter rotating flow), the Coriolis parameter f is nonzero, and an additional parameter enters the problem, namely the Rossby number U/fL, where L is the mountain half-width in the streamwise direction.

In two dimensional, nonrotating, high Nh/U flow, strong nonlinear effects associated with gravity wave breaking emerge and the flow may enter a high-drag state. This has been studied by numerical experiments by Clark and Peltier (1977, 1984), Peltier and Clark (1979, 1983), Durran (1986), Stein (1992b), and others. In recent years, there has been a growing interest in three-dimensional effects. Smith (1989a,b) has shown that linear theory predicts flow stagnation aloft and on the upstream slope of a mountain. The former leads to wave breaking and the latter to upstream blocking. When a blocked stage is reached, the flow is to a great

Corresponding author address: Dr. Haraldur Ólafsson, CNRM/Relief, Météo-France, 42, Avenue G. Coriolis, F-31057 Toulouse Cedex, France.
E-mail: olafsson@xdata.cnrm.meteo.fr

extent diverted to each side of the mountain, instead of over it. We shall refer to this as split (or blocked) flow. In such flows, the low-level isentropes do not any longer follow the topography, but intersect it and the low-level flow is no longer simply connected. Eliassen (1980) has characterized obstacles in such flows as ''warm.'' Thorsteinsson (1988) investigated the sensitivity of the descent of warm air in the lee upon Nh/U and U/fL. He did not study the mountain drag explicitly, but he found the magnitude of the warm zone in the lee to increase for constant Nh/U and increasing U/fL and also for constant U/fL and increasing Nh/U. The drag for nonrotating, high Nh/U flow around three-dimensional obstacles has been studied by Miranda and James (1992) and Stein (1992a). Their work constitutes one of our principal references and will be discussed in section 4.

The influence of surface roughness on mountain waves has been studied in two dimensions by Richard et al. (1989) and in three dimensions by Georgelin et al. (1994). Both found increasing roughness to reduce the mountain waves. On the other hand, Bougeault (1994) has discussed 2D simulations of orographic flow, including surface friction. He found the wave amplitude to be grossly underestimated in the absence of the Coriolis force and the large-scale pressure gradient. However, when these terms were introduced, the 2D result became remarkably close to a rather realistic 3D reference simulation. This result has motivated the present study.

The purpose of this paper is to investigate the magnitude of orographic drag, its three-dimensional structure, and its dependence on the nondimensional mountain height, the presence of a large-scale pressure gradient balanced by the Coriolis force, the surface friction, and the mountain aspect ratio. We simulate idealized as well as real flows as they meet an orographic obstacle. Our idealized flows have a uniform vertical profile of wind and stability and encounter a smooth, analytic mountain. Numerical experiments of the idealized flows have been conducted for $0.500 \leq Nh/U \leq 4.545$ and for $U/fL = 2.5$ and ∞. In the case of $U/fL = 2.5$, the upstream flow is in geostrophic equilibrium, and the flow may be considered as forced by dynamic sources. In the case of $f = 0$, the flow is forced only by the boundary conditions. In the first case, both free-slip as well as no-slip conditions at the surface have been simulated. We have concentrated mostly on flow past an elliptic mountain ridge with aspect ratio 5, in order to compare to cases from PYREX. However, in order to connect our results to existing theory and to study the effect of mountain aspect ratio, some experiments have been performed using a circular mountain. Finally, we present results from a case of real flow, simulated with and without surface friction and also without the dynamic sources. This case comes from the PYREX campaign, that took place around the Pyrénées in 1990.

2. The numerical model

A version of the PERIDOT limited-area model of Météo-France is used in this study (Imbard et al. 1986; Bougeault et al. 1991). PERIDOT is a primitive equation, hydrostatic model with a terrain-following vertical coordinate $\sigma = P/P_s$. The prognostic variables are the horizontal wind components U and V, the temperature T, and the logarithm of the surface pressure $Z = \log(P_s)$. In addition, the model carries the specific humidity, but this has been set to zero in all our present simulations. The model equations are as follows:

$$\frac{\partial Z}{\partial t} = -\frac{1}{P_s}\left\{\frac{\partial (P_s U)}{\partial x} + \frac{\partial (P_s V)}{\partial y} + \frac{\partial (P_s \dot{\sigma})}{\partial \sigma}\right\} - K_D(Z - Z_b) \tag{1}$$

$$\frac{\partial T}{\partial t} = -U\frac{\partial T}{\partial x} - V\frac{\partial T}{\partial y} - \dot{\sigma}\frac{\partial T}{\partial \sigma} + \frac{\omega}{p}\frac{R_a}{C_p}T + \left\{\frac{\partial T}{\partial t}\right\}_V + \left\{\frac{\partial T}{\partial t}\right\}_H - K_D(T - T_b) \tag{2}$$

$$\frac{\partial U}{\partial t} = -U\frac{\partial U}{\partial x} - V\frac{\partial U}{\partial y} - \dot{\sigma}\frac{\partial U}{\partial \sigma} - \frac{\partial \phi}{\partial x} + fV - R_a T\frac{\partial Z}{\partial x} + \left\{\frac{\partial U}{\partial t}\right\}_V + \left\{\frac{\partial U}{\partial t}\right\}_H - K_D(U - U_b) \tag{3}$$

$$\frac{\partial V}{\partial t} = -U\frac{\partial V}{\partial x} - V\frac{\partial V}{\partial y} - \dot{\sigma}\frac{\partial V}{\partial \sigma} - \frac{\partial \phi}{\partial y} - fU - R_a T\frac{\partial Z}{\partial y} + \left\{\frac{\partial V}{\partial t}\right\}_V + \left\{\frac{\partial V}{\partial t}\right\}_H - K_D(V - V_b). \tag{4}$$

Here, $\dot{\sigma}$ is the vertical velocity, ϕ is the geopotential height, and the subscripts V and H denote vertical and horizontal diffusion. The subscript b denotes boundary values, and the coefficient K_D determines a rate of relaxation toward the boundary values.

To calculate the geopotential we use the hydrostatic approximation:

$$\phi = \phi_s - \int_0^{\log \sigma} RT\, d(\log \sigma). \tag{5}$$

The horizontal discretization is on the Arakawa C-grid and the time discretization uses the leapfrog method and a weak Asselin filter.

To prevent wave reflection, a Rayleigh damping layer is placed above the height of two vertical wavelengths (12 570 m). The wave absorbtion coefficient increases with altitude according to the representation described by Klemp and Lilly (1978).

In addition, we have a prognostic equation for the turbulence kinetic energy (TKE)

TABLE 1. Overview of the simulations discussed in this paper.

$R = L_y/L_x$	Nh/U	Forcing only by b.c.	$\nabla P \neq 0, f \neq 0$, no surf.fric.	$\nabla P \neq 0, f \neq 0$, surf.fric.
5	0.500	EX05	EX05P	EX05PF
5	1.000	EX10	EX10P	EX10PF
				EX10PFa
5	1.400	EX14	EX14P	EX14PF
5	2.273	EX22	EX22P	EX22PF
5	2.700	EX27	EX27P	EX27PF
5	4.545	EX45	EX45P	EX45PF
1	1.000	EX10c	EX10cP	EX10cPF
1	2.700	EX27c	EX27cP	EX27cPF

$$\frac{\partial e}{\partial t} = -u\frac{\partial e}{\partial x} - v\frac{\partial e}{\partial y} - \dot{\sigma}\frac{\partial e}{\partial \sigma} - \frac{1}{\rho}\frac{\partial}{\partial z}\overline{\rho w' e'} - \overline{w'u'}\frac{\partial u}{\partial z} - \overline{w'v'}\frac{\partial v}{\partial z} + \beta\overline{w'\theta'} - \epsilon. \quad (6)$$

The terms in this equation are the horizontal and the vertical advection, the turbulent transport, the production by vertical wind shear, the buoyancy term, and the dissipation. The dissipation is estimated by the relation $\varepsilon = C_\varepsilon e^{3/2}/l_\varepsilon$, where C_ε is an $O(1)$ numerical coefficient, and l_ε is a characteristic length of the energy-containing eddies. The eddy coefficients are related to the turbulence kinetic energy through $K = C_k l_k \sqrt{e}$, where C_k is a constant, l_k is a vertical length scale, and e is the turbulence kinetic energy. For our free-slip flows, high concentrations of TKE are mainly found aloft, in relation to wave breaking, while in simulations with a rough surface, the wave breaking is suppressed, and the TKE is mainly found near the surface, generated by shear production.

The turbulence scheme has been shown to give realistic results for convective situations and breaking waves (Bougeault and Lacarrère 1989) and for quasi-neutral flow (Masson and Bougeault 1996). The adiabatic part of PERIDOT has also been validated for two-dimensional as well as three-dimensional orographic flows by Stein (1992a).

Dimensional analysis of Eq. (6) reveals dependence on a horizontal length scale, and the Nh/U similarity is strictly not valid for the turbulence scheme. However, Ólafsson and Bougeault (1996) have tested the similarity by simulating flows with different combinations of parameters, giving the same nondimensional height, and they found only minor deviations from the similarity.

3. Description of the simulations

Table 1 gives an overview of the simulations presented in this paper. The numbers in the name of each experiment refer to the value of the nondimensional mountain height, and the following letters refer to how the flow is forced and whether there is surface friction or not. Example: EX10 refers to flow with $Nh/U = 1.0$, forced only by the boundary conditions, EX14P has flow with $Nh/U = 1.4$, forced by a large-scale pressure gradient, balanced by the Coriolis force, but no surface friction (free slip). EX27PF has flow with the $Nh/U = 2.7$, forced by a large-scale pressure gradient, balanced by the Coriolis force, and with surface friction (no slip). EX10PFa is as EX10PF, but with $z_0 = 0.1$ m everywhere at the surface. An extended collection of the flow fields in the simulations described in Table 1 has appeared in Ólafsson (1996).

The simulations were run with 40 levels on a 10-km grid. The horizontal domain consists of 121×121 points for a mountain with aspect ratio 5, and 61×61 points for a circular mountain. The mountain height is given by

$$h(x, y) = h_{\max} \Big/ \left[1 + \left(\frac{x}{L_x}\right)^2 + \left(\frac{y}{L_y}\right)^2\right]^{1.5}, \quad (7)$$

where $h_{\max}$ (hereafter h) is the mountain top height, and L_x, L_y are the mountain half-widths in the streamwise and cross-stream directions, respectively. This mountain shape has been used by Smith (1980, 1989b), Phillips (1984), Smolarkiewicz and Rotunno (1989, 1990), and others for different aspect ratios. Here, we set L_x to 40 km and L_y to 200 km, since we are mainly interested in interpretating observations taken over the Pyrénées. This gives $R = L_y/L_x = 5$. For simulations with a circular mountain, we set $L_x = L_y = 40$ km.

The model is initialized everywhere with $U = 10$ m s^{-1} along the x axis and $N = 0.01$ s^{-1}. The lateral boundary conditions are the same as the initial conditions, and they are constant in time. The nondimensional mountain height Nh/U is changed through h. Thus, high Nh/U goes together with a high mountain. Keeping L_x and L_y constant, we therefore also get a steeper mountain as Nh/U is increased. The numerical setup described here has been thoroughly validated for flows with $f = 0$ (Ólafsson and Bougeault 1996).

Simulations with the Coriolis force have $f = 10^{-4}$ s^{-1}, thus $U/fL = 2.5$. The geostrophic balance has been verified by checking that the flow is steady in the absence of an obstacle. Simulations with surface friction have an Ekman spiral in the lowest 1000 m, at the boundaries as well as in the initial field. This Ekman spiral is obtained by simulating flow over flat ground with a roughness length $z_0 = 0.1$ m, until stationarity is reached. The total wind turning in the Ekman layer is 26°.

In real atmospheric conditions, we may in general expect the value of the roughness length to be more or less proportional to the height of the mountain. In our simulations with surface friction, we set $z_0(x, y) = \max[0.1 \text{ m}, 0.556h(x, y)]$, except in EX10PFa, where $z_0(x, y) = 0.1$ m. This gives $z_0 = 15$ m for $h = 2700$ m, a reasonable value for the Pyrénées (Georgelin et al. 1994). It should be noted that we cannot expect the Froude and Rossby number similarity to remain strictly

valid when surface friction is present. The value for the nondimensional frictional drag coefficient C_D is 4.38×10^{-3} on the plane and in EX10PFa. The maximum value of C_D ranges from 2.21×10^{-2} in EX05PF to 1.10 in EX45PF. By scaling the equation of horizontal momentum and considering the proportion of advection to friction, we obtain a nondimensional frictional number $\hat{f} = C_D N\, L/U$. In all our simulations, $NL/U = 40$ and the values of $\hat{f}$ corresponding to the above values for C_D are 0.175, 0.884, and 44.0.

In less than six nondimensional time units ($t^* = Ut/L_x$), the drag has reached a value that is close to stationary. All main features of the nonrotating flows have reached a stationary state in less than 10 nondimensional time units, but with small fluctuations in, for instance, surface pressure and wind speed. In simulations with the Coriolis force present, instabilities occur in the wake of the mountain. These instabilities, characterized by vortex shedding, do not have a large impact on the surface pressure drag. The observed fluctuations may relate to the quasi-stationary nature of wave breaking, which oscillates between the phase of wave buildup and breaking. Other processes in the flow, such as small vortex development inside the upstream blocking may also have a quasi-stationary, oscillating nature. In EX27P (blocked flow with weak wave breaking), we observe fluctuations of $\pm 4\%$ in the drag, while in EX10P (unblocked flow with stronger wave breaking) the fluctuations in the value of the drag are $\pm 8\%$. These fluctuations are smaller than simulated by Miranda and James (1992) for a flow around a circular mountain in a high-drag state. The aim of this paper is not to study the oscillations as such, but the overall magnitude of the drag for different settings. In general, the governing parameters induce changes in the drag that are of much greater magnitude than the aforementioned oscillations. In the following sections, we discuss results at $t^* = 16.2$. At that time, the flow is sufficiently stationary for the present purposes.

4. Previous results on mountain drag

The pressure drag force exerted by the airflow on the mountain in the x direction can be expressed as

$$\mathcal{D} = \int_{-\infty}^{+\infty} \int_{-\infty}^{+\infty} p' \frac{\partial h(x, y)}{\partial x}\, dx\, dy, \tag{8}$$

where p' is the pressure anomaly and $h(x, y)$ is the mountain height.

For frictionless, inviscid, and nonrotating flow, this force is often conceptually divided in two components: the wave drag and the drag due to accumulation of cold air on the upstream slope of the mountain and warm air in the lee. The latter is sometimes referred to as ''hydrostatic drag,'' although this expression is preferably used for the total pressure drag computed by a hydrostatic model (e.g., Miranda and James 1992).

Several analytic expressions are known for hydrostatic, linear, Boussinesq flow with no surface friction. The drag produced in nonrotating conditions by an infinite, two-dimensional bell-shaped mountain on a slice of flow of width L_y is given by the well-known formula

$$\mathcal{D}_{\text{2D,lin}} = \frac{1}{4} \pi \rho_0 NUh^2 \times L_y. \tag{9}$$

Here, ρ_0 is the mean density. Equation (9) is also valid for one period of a sinusoidal mountain. Bessemoulin et al. (1993) found this expression to predict the drag observed during PYREX in the central section of the Pyrénées surprisingly well, although the flow conditions were far from linear and 2D. They did not propose an explanation of this.

In the presence of rotation, the drag takes a smaller value. For an infinite, 2D, bell-shaped mountain the analytic expression is (e.g., Gill 1982, 281)

$$\mathcal{D}_{\text{2D,lin},\, f} = \frac{1}{2} \pi \rho_0 Nh^2 LfK_1(2Lf/U) \times L_y. \tag{10}$$

Here, L is the mountain half-width, and K_1 is an elliptic function. For small f, the above expression approaches asymptotically the nonrotating value of Eq. (9). For increasing f, the drag decreases.

Another interesting relation has been derived by Smith (1979):

$$\mathcal{D}_{\text{2D,lin},f} = \left[-\rho_0 \int_{-\infty}^{+\infty} u'w'\, dx - f\rho_0 \int_{-\infty}^{+\infty} \eta' v'\, dx \right] \times L_y. \tag{11}$$

Here, the mean density ρ_0 and Coriolis parameter f are taken to be constant; u', w', and v' are perturbation velocities; and η' is the height of a streamline above its undisturbed level. The first integral is the vertical flux of momentum, and the second is the Coriolis force acting in the region between the undisturbed streamline level and the vertically displaced streamline. In Eq. (11), the first term is in general positive, while in the second term, η' and v' are correlated in such a way that the term is negative. In other words, the Coriolis force acts to reduce the drag.

Analytical expressions for the total pressure drag for three-dimensional obstacles of different aspect ratio with no Coriolis force have been derived by Phillips (1984). He found the total drag on the barrier in the direction of the flow to be given by

$$D_{\text{3D,lin}} = \rho_0 NUh^2 L_y G(B \cos^2\psi + C \sin^2\psi), \tag{12}$$

where L_y is now the mountain half-width transverse to the upstream flow, G is a function of mountain shape, and ψ is the angle between x and the upstream flow. B and C are combinations of elliptic integrals of the mountain aspect ratio. In our case, $L_y = 200$ km, $G = 1$, $\psi = 0$, giving $C \sin(\psi) = 0$, and $B = 0.97$ [accounting for an error in Phillips'(1984) Eq. (4.4), where the de-

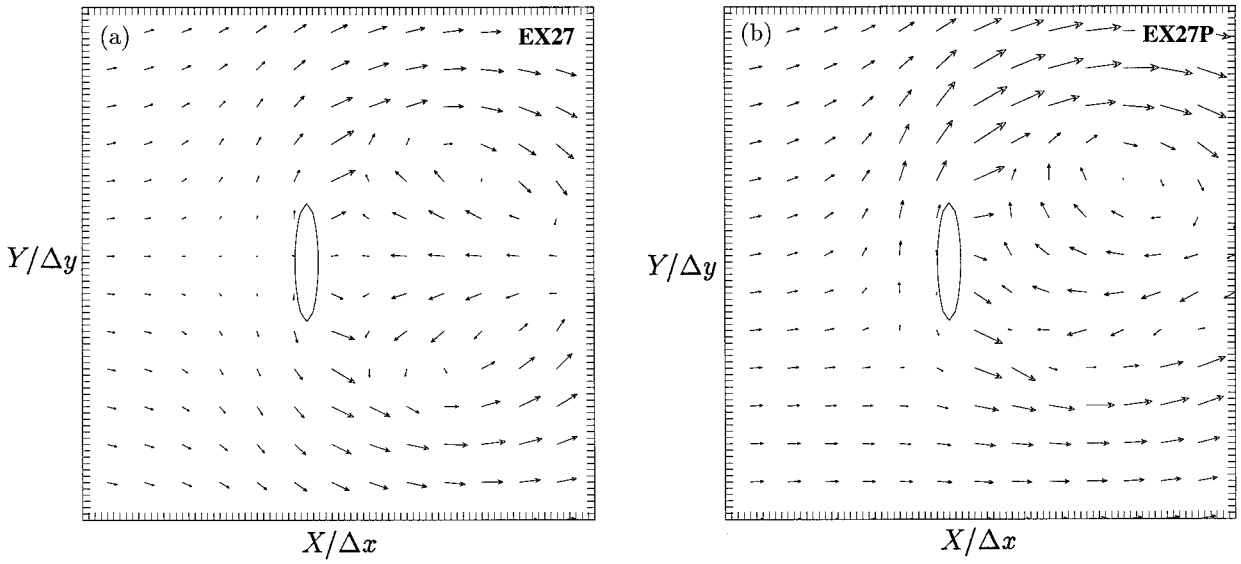

FIG. 1. The surface flow in EX27 (a) and in EX27P (b).

nominators should be squared]. The value of B for a circular mountain is 0.78. Our three-dimensional calculations of drag will be normalized by Eq. (9).

For the nonlinear regime, analytic expressions do not seem to exist. Miranda and James (1992) and Stein (1992a) have carried out numerical studies of the drag at high Nh/U on a nonrotating plane. Miranda and James (1992) found the maximum drag [normalized by the linear value of Eq. (9)] for a circular mountain to occur near $Nh/U = 1.5$. This is in fair agreement with the corresponding value of 1.4 found by Stein (1992a). Near this value of Nh/U, Miranda and James observe wave breaking above the lee slope, but the upstream flow still remains unblocked. As the nondimensional height is increased, the flow splits and wave breaking dies out. This coincides with a rapid decrease in the normalized drag. At $Nh/U = 2$, the drag has decreased to the value predicted by linear hydrostatic theory, and for $Nh/U = 4$, the drag has only about half its linear value. At this stage, there is no wave breaking and the flow is highly split. Their results are nearly unchanged when using a hydrostatic version of their model. This lends credence to our present, hydrostatic simulations.

Stein (1992a) investigated the effect of mountain aspect ratio on the evolution of the drag for Nh/U in the range of the regime transition to wave breaking and flow splitting. He found the maximum drag for a mountain ridge with aspect ratio 5 to be near $Nh/U = 1.0$. This is significantly less than the corresponding value for a circular mountain. Furthermore, in the case of the mountain ridge ($R = 5$), the normalized drag is greater in the high-drag state than for a circular mountain. The decrease in the drag for increasing value of Nh/U is slower for a mountain ridge, and the linear value is not reached until $4.0 < Nh/U < 4.5$. Stein also found that, for a 3D mountain and flow in the high-drag state, the increase in drag is rapid for aspect ratio growing from 1–2, while for higher aspect ratio there is only a little increase in the drag.

We now move on to discuss our present results.

5. Idealized flows

a. Influence of the Coriolis force on the flow pattern

The morphology of the flow in the cases of interest, with no rotation, has been discussed in several previous papers (e.g., Smolarkiewicz and Rotunno 1989, 1990; Stein 1992a; Ólafsson and Bougeault 1996). When the Coriolis force is introduced, the left–right symmetry of the flow is broken. Figure 1 compares the surface flow in EX27 and EX27P. The flow in EX27P is to a greater extent diverted to the left (facing downstream), giving greater wind speeds than on the right side of the mountain. The flow in the wake is unstable, and we observe vortex shedding in our simulations. This is in agreement with Schär and Smith (1993) and Sun and Chern (1994).

Figure 2 shows how the asymmetry in the flow affects the wave structure. In a cross section located one L_y to the left of the centerplane (Fig. 2b), the wave is steep and strong turbulence (not shown) indicates breaking or near breaking. On the other hand, the wave one L_y to the right of the centerplane (Fig. 2c) is less steep and little turbulence is detected. In fact, we find that the wave on the right side in EX27P is very similar to the waves one L_y away from the centerplane in EX27, without rotation, shown in Fig. 2a. In short, we find the introduction of the Coriolis force to have significant effect on the flow, especially by favoring wind and wave steepening on the left side of the centerplane.

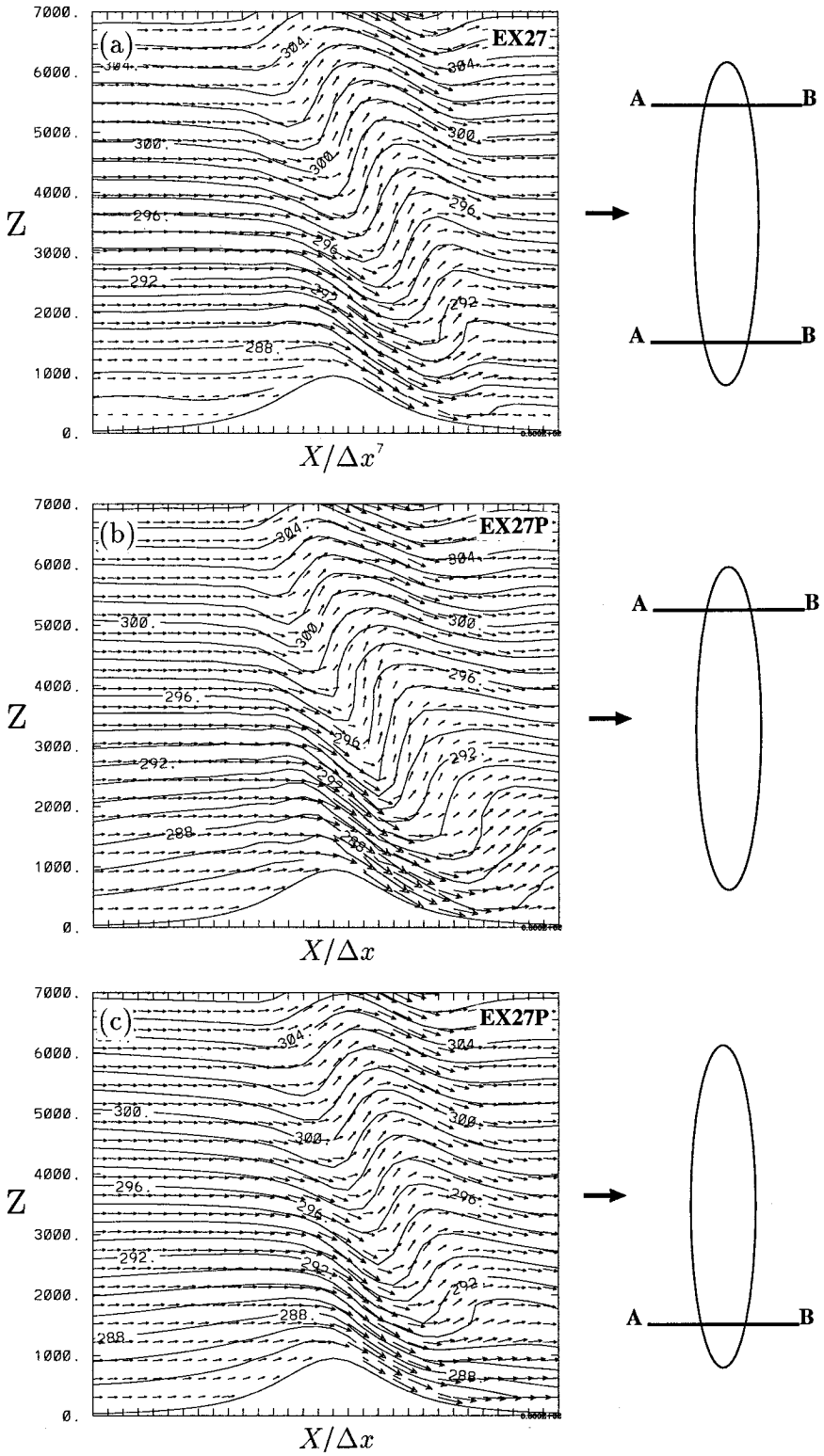

FIG. 2. Potential temperature and wind in vertical cross sections located (a) in EX27, one L_y away from the centerplane; (b) in EX27P one L_y to the left of the centerplane; (c) in EX27P one L_y to the right of the centerplane. Here, Z is in meters.

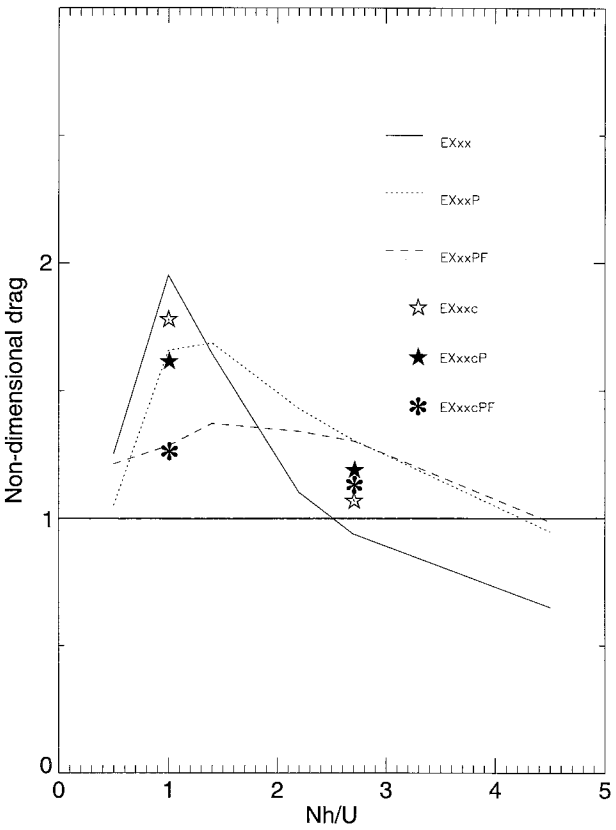

FIG. 3. Nondimensional drag in the direction along the upstream flow as a function of Nh/U. The lines show the drag for $R = 5$ and the points at $Nh/U = 1.0$ and 2.7 show the drag for $R = 1$. The drag is normalized with Eq. (12), with $G = 1$, $B = 0.78$ for $R = 1$, and 0.97 for $R = 5$.

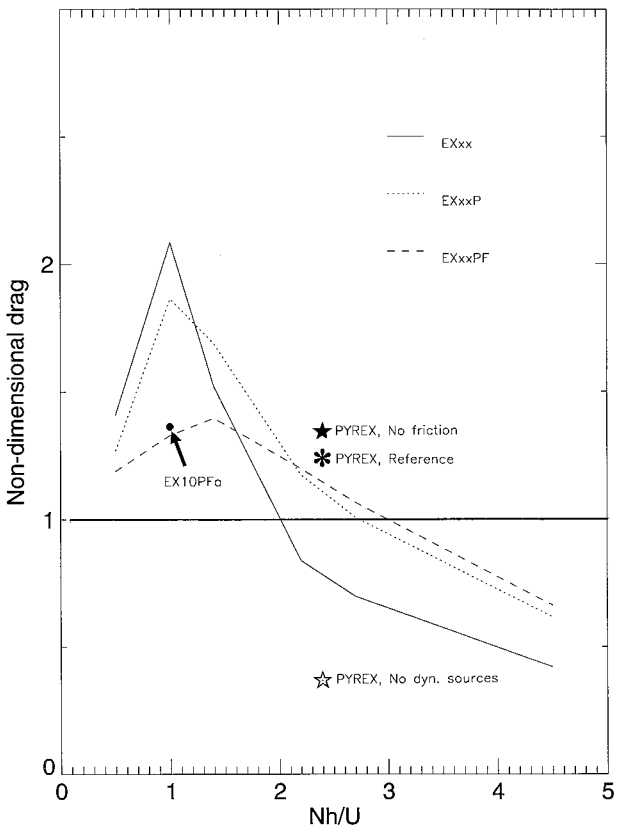

FIG. 4. Nondimensional drag along the central cross section as a function of Nh/U, for the $R = 5$ mountain. The simulated values of the drag in a cross section along the central part of the Pyrénées on 16.11.90 at 0900 UTC are also given ($\overline{Nh/U} = 2.4$). The drag is normalized with Eq. (9).

b. Overall drag behavior

The total drag in the x direction for our experiments is shown in Fig. 3. This figure summarizes the main results of the present paper. All drag values are normalized by the nonrotating, linear expression of Phillips [Eq. (12)]. The overall behavior is similar to that found by Miranda and James (1992) and Stein (1992a). It exhibits the occurrence of a maximum of normalized drag when Nh/U increases, followed by a regular decrease. At large Nh/U, the normalized drag falls below 1.

The main novelty of the present results lies in the large differences between the three curves in Fig. 3. At low Nh/U, the simulations with no rotation give the greatest drag, while the simulations including surface friction have the smallest drag. For higher values of Nh/U, the situation is exactly inversed: the nonrotating flow gives the lowest value of the drag, while simulations with rotation and surface friction is on top, with a slightly greater value than rotating flow, without surface friction. For $Nh/U \geq 2.7$, the nonrotating flow gives only about 70% of the drag in the rotating flow. We note that the curves in Fig. 3 intersect each other for Nh/U between 1.0 and 1.4. This is approximately where we may expect the onset of flow splitting, following Smith (1989a).

Another look at the same phenomenon is taken in Fig. 4 where the drag along the central cross section, normalized by Eq. (9), is shown. It is obvious that Figs. 3 and 4 convey similar information. At high values of Nh/U, the drag on an f plane is greater than for $f = 0$. In fact, EX27 has only 72% of the drag of EX27P. This is opposite to what may be expected from Eq. (10) and Eq. (11). On the other hand, at lower values of Nh/U, the drag is less for $f \neq 0$ than for $f = 0$. This is qualitatively in agreement with Eq. (10) and Eq. (11). The 2D, linear value of the normalized drag in the rotating case, evaluated from Eq. (10) with $U/fL = 2.5$, is 81% of the $f = 0$ value. In our numerical experiment with $R = 5$, we found the corresponding factors in the central cross section to be 90% for $Nh/U = 0.5$ and 89% for $Nh/U = 1.0$ (from Fig. 4). The difference between the theoretical and numerical result may be due to 3D or nonlinear effects. Furthermore, we note that the onset of wave breaking (near $Nh/U = 1.0$) has only little effect on the drag reduction due to rotation.

The values of the drag for a circular mountain at $Nh/U = 1.0$ and $Nh/U = 2.7$ are also given in Fig. 3. In

general, the evolution of the drag as a function of Nh/U appears similar for $R = 1$ and $R = 5$. As for $R = 5$, the simulation with no rotation gives the greatest drag for $Nh/U = 1.0$, while the simulation with surface friction gives the lowest value of the three. At $Nh/U = 2.7$, the drag for the simulation without rotation has moved from the top to the bottom of the three and the simulation with surface friction has a little less drag than the free-slip, rotating simulation. We note that the values of the drag for the different simulations is more alike for $R = 1$ than for $R = 5$. While EX27 gives only 72% of the drag in EX27P, EX27c gives 90% of the drag in EX27cP. This indicates that the effects that govern the different behavior with and without rotation are more important for high aspect ratio.

c. *Interpretation of the drag behavior at high nondimensional height*

While the effect of the rotation is qualitatively in agreement with linear theory until $Nh/U \simeq 1.4$, we have noted in the previous sections an opposite behavior at higher values of the nondimensional mountain height. A simple explanation of this can be found by considering at first order the combined effect of the large-scale pressure gradient and the Coriolis force as a relaxation toward the mean geostrophic flow. For unblocked flow at low Nh/U, acceleration above the mountain dominates the flow field and therefore the flow is slowed by the effect of rotation. For blocked flow (high Nh/U), the flow field is dominated by the deceleration in the blocking, and here the rotation acts to accelerate the flow. This argumentation agrees with Pierrehumbert and Wyman (1985). On a nonrotating plane, they found that the upstream deceleration extended arbitrarily far upstream of an infinitely long mountain ridge, while if rotation was present, the decelerated zone propagated only a limited distance upstream.

In section 4 we presented analytic solutions that predict a reduction of the drag in the presence of the Coriolis force. This can be understood physically by considering the fluid being decelerated as it approaches the mountain. The deceleration weakens the Coriolis force, and there is a net force acting to turn the flow left. From an energetic point of view, kinetic energy is transferred from flow in the x direction (u) to flow in the y direction (v). The source of kinetic energy that counteracts the buoyancy force and forms the mountain wave, comes from the movement along the x axis, and consequently one may expect less pronounced waves in the presence of Coriolis force. Similar arguments may be used for flow with high Nh/U, but for such blocked flows the drag increase by accumulation of low-level dense air is more important than the reduction of wave drag and the result is a net drag increase.

The accelerating effect of rotation on the blocked flow suggests that the presence of the Coriolis force may delay the onset of flow splitting. To test this, we compare

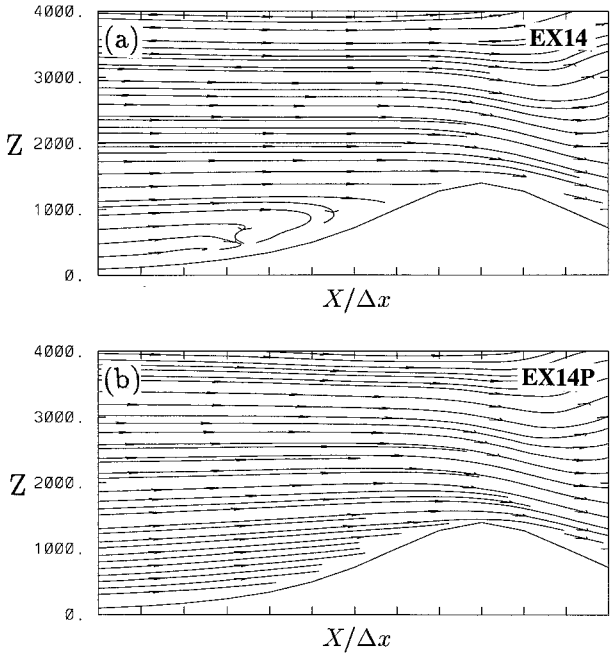

FIG. 5. Streamlines in the centerplane showing (a) blocked flow in EX14 and (b) unblocked flow in EX14P. Z is in meters.

the upstream flow at $Nh/U = 1.4$ for nonrotating flow (EX14) and rotating flow (EX14P). Figure 5 shows indeed that in EX14 there is stagnation and reversed flow on the upstream slope, while the flow in EX14P does not stagnate. This is an interesting result, since flow with $Nh/U = 1.4$ and aspect ratio 5 is well within the zone of flow splitting on Smith's (1989a) regime diagram.

d. *Pressure distribution in the central section*

Let us now take a closer look at the different simulations for two particular values of Nh/U, one at $Nh/U = 2.7$, giving split flow and weak wave breaking and the other at $Nh/U = 1.0$, giving high drag and strong wave breaking, but no flow splitting. EX27 and EX27P (Figs.6a and 6b) show similar wave activity aloft. We suspect therefore that the drag difference is due to differences in density of the low-level flow, and indeed, we find EX27P to have more accumulation of low-level dense air above the upstream slope of the mountain (see, e.g., the 288K isentrope). A comparison of the pressure pattern in the centerplane (Fig. 7) shows greater pressure anomaly on the upstream side in the simulations of rotating flows. On the lee side, we find the pressure anomalies to be more similar in these two simulations, and contrary to the upstream conditions, EX27 gives a slightly greater pressure anomaly. Figure 8, showing the pressure anomalies at $Nh/U = 1.0$ gives quite a different pattern. Here, the upstream anomalies of EX10 coincide with EX10P just upstream of the mountain top, while further upstream EX10 has greater pressure. In the lee,

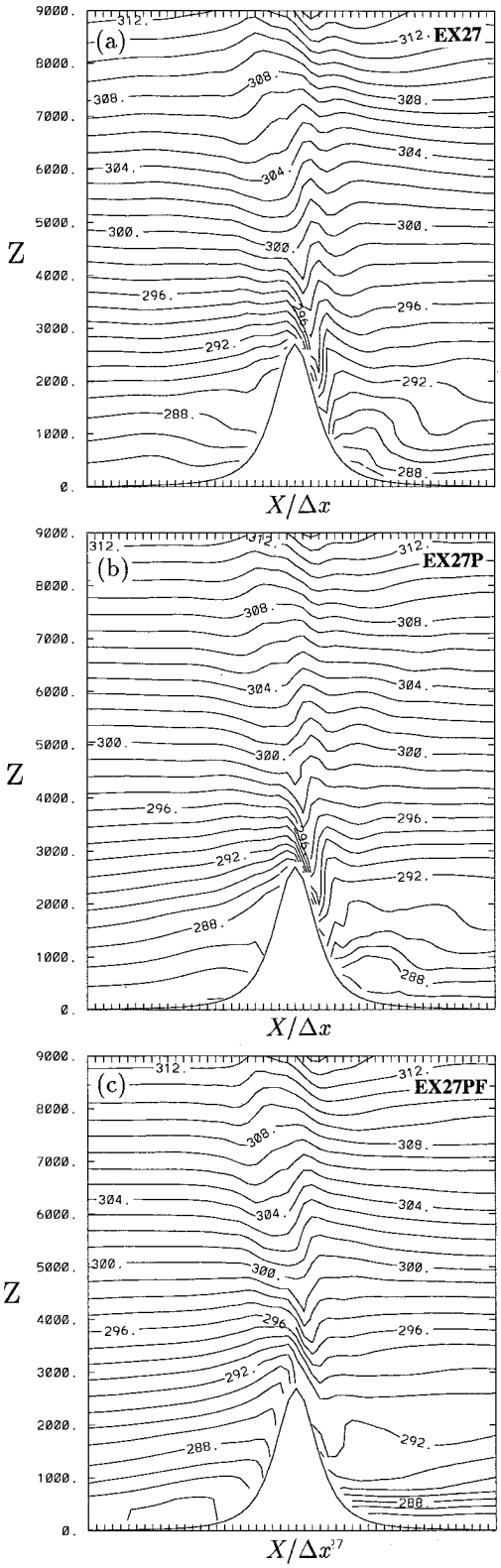

FIG. 6. Potential temperature in cross sections along the centerplane in (a) EX27, (b) EX27P, and (c) EX27PF. Here, Z is in meters.

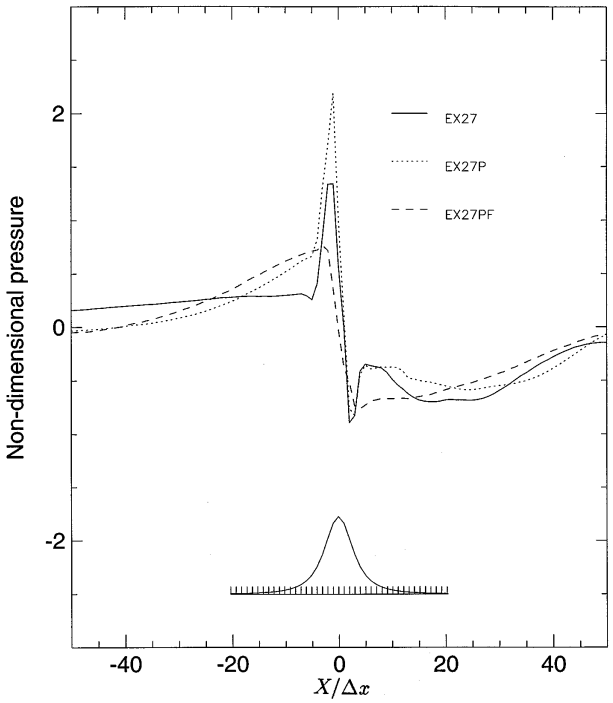

FIG. 7. Nondimensional surface pressure perturbation in the centerplane in EX27, EX27P, and EX27PF, with the mountain profile shown below. The pressure is normalized with $\rho_0 NUh$. The flow is from left to right.

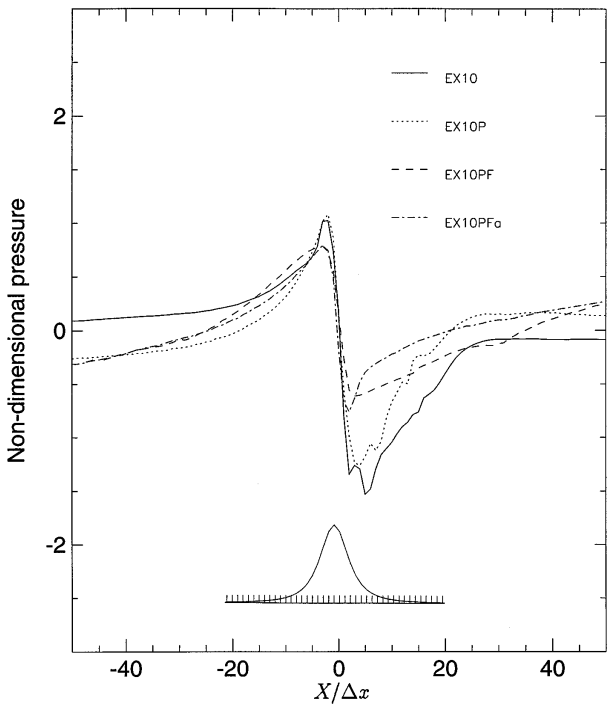

FIG. 8. Nondimensional surface pressure perturbation in the centerplane in EX10, EX10P, EX10PF, with the mountain profile shown below. The pressure is normalized with $\rho_0 NUh$. The flow is from left to right.

EX10 features a somewhat greater pressure anomaly than EX10P, both immediately behind the mountain top as well as further downstream. Thus, both sides of the mountain contribute to greater drag in EX10, compared to EX10P. The wave pattern in these simulations is given in Fig. 9. In EX10P, there is steeper rise in the lowest isentropes above the upstream slope, leaving less dense air at the foot of the mountain, than in EX10. Above the lee slope, EX10 has somewhat steeper waves and there is sligthly warmer air than in EX10P. This is in agreement with Thorsteinsson (1988), who studied the collapse of isentropes on the lee slope, leading to increased temperature in the wake of a circular mountain. For increasing U/fL, he found the wake to grow warmer.

e. Left–right asymmetry

We now examine the distribution of the drag in the y–z plane perpendicular to the upstream flow for two specific cases. This is displayed in Fig. 10 for $Nh/U = 2.7$, $R = 5$, and in Fig. 11 for $Nh/U = 2.7$, $R = 1$. In these figures, the mountain is supposed to be viewed from upstream. For the rotating flows, the drag curves are displaced to the right with respect to the topography and the drag in the nonrotating flows. This must be related to the Coriolis force and the asymmetry in the flow field. The lower drag on the left-hand side of the centerplane is surprising, because this is the side where the mountain wave is steeper, and breaking is present. Some explanation of this fact may be provided by Eq. (11), although it is valid for 2D, linear flow, and our flow is 3D and highly nonlinear. We could indeed verify, by post-processing our model results, that the first term in (11), that describes the wave momentum flux, is greater on the left than on the right-hand side, while the second term, involving the Coriolis force, is negative and has larger variations between the left and the right side.

The pressure curves given in Fig. 12 reveal that the asymmetry is mainly due to lower pressure on the right side, in the lee. The upstream pressure anomalies are also asymmetric, but in the opposite direction. Here, the left-side anomaly is greater than the one on the right side. In the lee, on both sides, there is a second pressure minimum far downstream of the mountain in the simulation without surface friction. These minima are too far from the mountain to contribute to the drag. They are related to the warm lee vortices and we note that the minima are eliminated by surface friction. Not unexpectedly, the lee pressure asymmetry is connected to the asymmetry of the flow in the wake. Returning to the horizontal flow in Fig. 1, we find the left vortex to be much stronger than the vortex on the right-hand side. Consequently, there is greater advection back toward the left part of the lee slope. The associated convergence in the horizontal flow field prevents the warm strata above the upper parts of the lee slope to extend further downstream. On the right-hand side, the horizontal flow is less convergent and the warm air is not as easily replaced by low-level dense air.

The comparison of the drag distribution in the y-z plane for $R = 1$ and $R = 5$ shows similar characteristics in both cases (Fig. 10 and Fig. 11). However, we note that the drag delivered by the different simulations is more alike for $R = 1$ than for $R = 5$. While EX27 gives only 72% of the drag in EX27P, EX27c gives 90% of the drag in EX27cP. The ratio of the total drag in the x direction exerted by the mountain ridge (EX27) to the drag of the circular mountain (EX27c) is 8.3. This is represented by the areas under the curves in the cross sections of Figs. 9 and 11, giving the total drag of the mountain. This is a larger difference than in Phillips' (1984) linear theory, which predicts a factor of 6.2.

f. The effect of surface friction

The most striking result of our simulations with surface friction is the effective suppression of wave activity and the complete absence of wave breaking for all tested values of Nh/U. This result is not entirely unexpected, since Elkhalfi and Richard (1993) found surface friction to have a comparable effect on 2D mountain wave drag in real flow. On the other hand, Richard et al. (1989) studied a downslope windstorm in real flow and found surface friction to have little impact on the wave drag once it had reached a steady state. They also found the impact of surface friction to be sensitive to the parameterization scheme. For 3D flow, Georgelin et al. (1994) have shown that increased roughness reduces the mountain wave amplitude. The flow pattern for $Nh/U = 1.0$ in the centerplane is shown in Fig. 9c. The suppression of wave activity is represented in the drag in Fig. 3 and Fig. 4, where the high-drag simulations with surface friction give much less drag than the free-slip flow. However, a study of the pressure curves in Fig. 8 shows, unlike EX10 and EX10P, a nice upstream–downstream symmetry for EX10PF. This symmetry is reminiscent of linear flow, and we note indeed that the wave magnitude in EX05P (Fig. 13) is similar to that obtained in EX10PF above the surface layer. Compared to EX10 and EX10P, EX10PF's lack of drag is mainly due to the reduced leeside pressure anomaly. This corresponds well with the large differences in the waves above the lee slope.

On the other hand, for high values of the nondimensional mountain height, corresponding to split flow, Figs. 3 and 4 show the no-slip simulations to give the greatest drag. The no-slip drag is slightly greater than the free-slip simulations with rotation and considerably greater than in the simulations without rotation. A study of the pressure curves for $Nh/U = 2.7$ in Fig. 7 shows that although EX27P and EX27PF give similar drag, the pressure patterns differ significantly. Just upstream of the mountain top, EX27PF has the smallest pressure value, while farther upstream it has somewhat greater pressure than EX27P. This pattern is similar as for $Nh/$

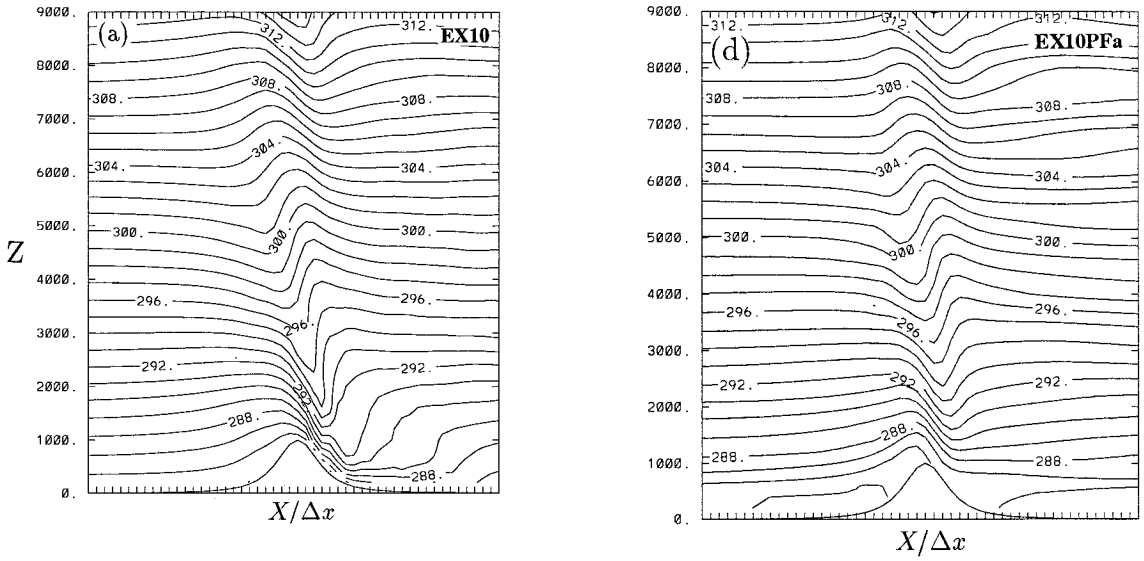

FIG. 9. Potential temperature in cross sections along the centerplane in (a) EX10, (b) EX10P, (c) EX10PF, and (d) EX10PFa. Here, Z is in meters.

$U = 1.0$, but here the differences are greater. In the lee, EX27PF reveals an interesting effect of surface friction. A deep and spatially extended low pressure region is created in the no-slip flow. In spite of the suppression of wave activity, this low is almost as deep as the narrow region of low pressure that develops in the free-slip flows. The extended low pressure region is related to divergence in the flow in the wake. As in linear theory, the horizontal divergence persists downstream of the mountain where surface friction is present. The divergent flow hinders the jumplike flow pattern, which appears in the free-slip flows (Figs. 6a and 6b). In other words, the warm air that has descended from above, over the upper part of the lee slope extends farther downstream, giving greater drag where surface friction is present (Fig. 6c).

Another interesting aspect of surface friction is that it generally brings the drag closer to its linear value. In the high drag state, the simulations with surface friction give much less drag than the free-slip simulations. In the blocked state, where the drag drops below the value predicted by linear theory, surface friction acts to increase the drag. Surface friction also gives a slight increase in the asymmetry of the drag in the cross section transverse to the flow.

To test the sensitivity to the mountain surface roughness, EX10PF was repeated, but with $z_0 = 0.1$ m ($C_D \times NL/U = 0.175$) everywhere (EX10PFa). This is a typical plane value of z_0 and far below what may be considered realistic in mountainous terrain. The resulting drag is given as a dot in Fig. 4, and we see that the low friction drag in EX10PFa is much closer to the EX10PF curve than to the free-slip flow in EX10P. This indicates little sensitivity to the surface friction param-

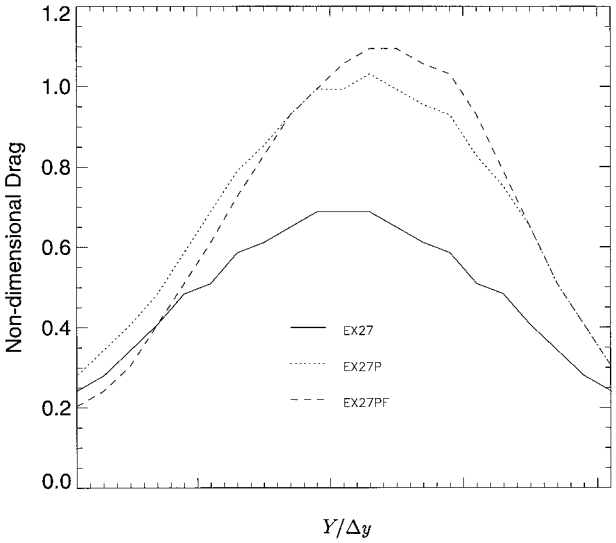

FIG. 10. Cross section along the *y* axis, showing the nondimensional drag in 2D sections along the flow in EX27, EX27P, and EX27PF. The drag is normalized with $\pi\rho_0 NUh^2/4$ (as elsewhere, *h* is the mountain-top height). The flow is into the page.

eterization. Investigating the wave pattern in EX10PF and EX10PFa reveals, however, steeper (though nonbreaking) waves in EX10PFa (Figs. 9c and 9d). Above the lower part of the upstream slope in EX10PF, there is on the other hand greater accumulation of low-level dense air, which acts to compensate for the loss of drag due to wave suppression. The pressure curves of EX10PF and EX10PFa in Fig. 8 illustrate this; EX10PF gives greater pressure above the lower parts of the upstream slope, while the pressure drop in the lee is greater in EX10PFa. Farther downstream, EX10PFa has a reduced pressure anomaly, which is associated with more convergence in the horizontal flow.

g. Summary

In summary, the combined effect of rotation at moderate Rossby number and surface friction on nonlinear

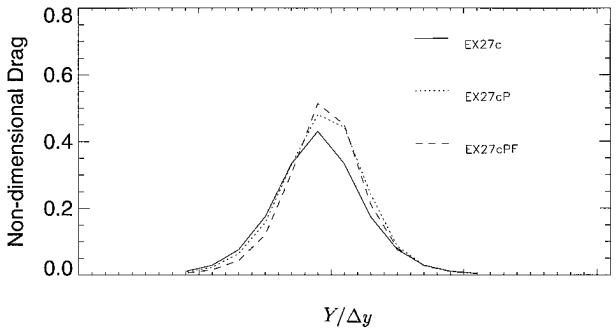

FIG. 11. Cross section along the *y* axis, showing the nondimensional drag in 2D sections along the flow for EX27c, EX27cP, and EX27cPF. The drag is normalized with $\pi\rho_0 NUh^2/4$ (as elsewhere, *h* is the mountain-top height). The flow is into the page.

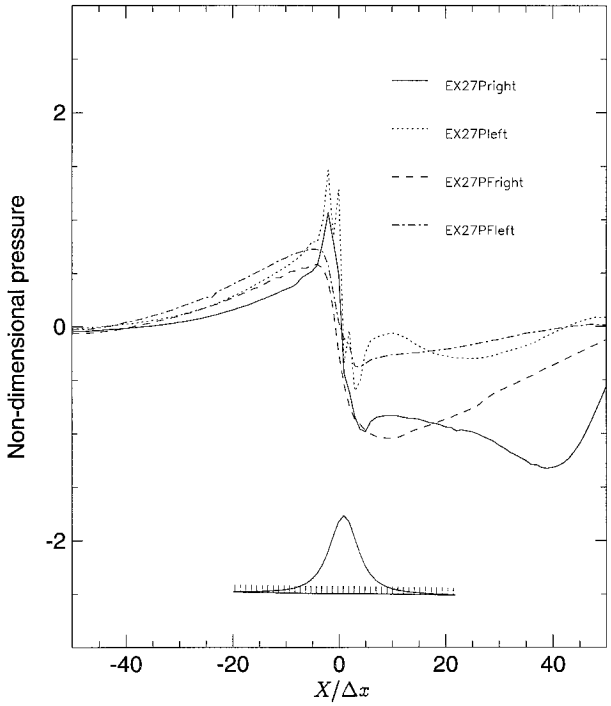

FIG. 12. Nondimensional surface pressure perturbation in cross sections $0.5L_y$ to the left and to the right of the centerplane in EX27P and EX27PF. The mountain profile is shown below. The pressure is normalized with $\rho_0 NUh$, and the flow is from left to right.

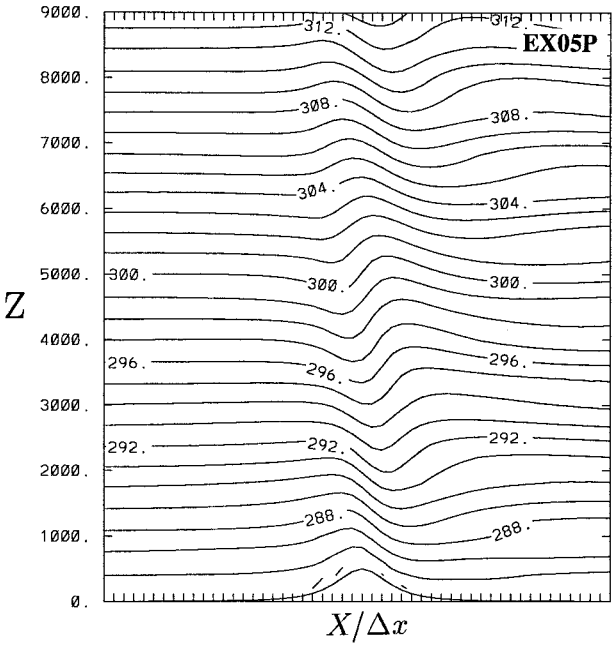

FIG. 13. Potential temperature in a cross section along the centerplane in EX05P. *Z* is in meters.

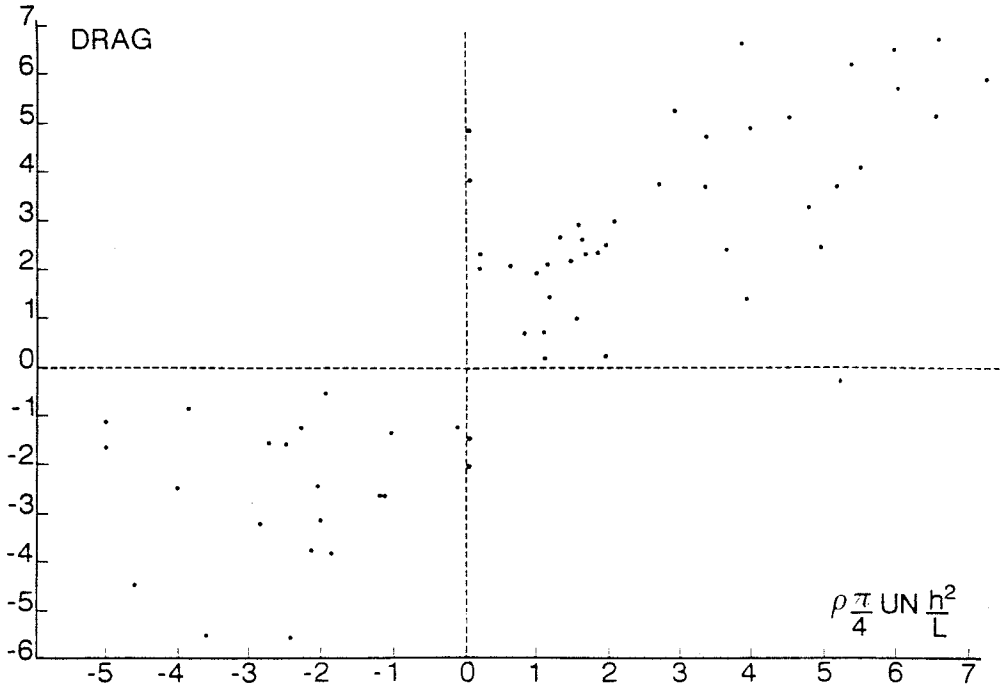

FIG. 14. Scatterplot of observed pressure drag against the 2D linear hydrostatic value for incoming airflow perpendicular to the Pyrénées (reproduced from Bessemoulin et al. 1993).

orographic flow is to always bring the drag to a value closer to its linear value (see Figs. 3 and 4), but this is achieved in contrasting ways. In the high-drag state, the drag is reduced by the rotation, and further reduced by the friction, but the main effect is due to the friction, in relation to the reduction of wave activity. In the blocked state, the drag is increased by the rotation, and further increased by friction, but the main effect is due to the rotation.

These results may help explain the recent experimental evidence of Bessemoulin et al. (1993). They found that the drag evaluated experimentally by high resolution pressure measurements in the central cross section of the Pyrénées during the PYREX field program (Bougeault et al. 1993) was in general well approximated by the most simple 2D, linear, nonrotating theoretical prediction of Eq. (9). This is shown in Fig. 14, reproduced from their paper. Needless to say, the flow conditions encountered during PYREX were highly nonlinear, three-dimensional, and the Rossby number U/fL had values comparable to our 2.5. The above-mentioned result had not yet been explained. In the light of the present simulations, we are inclined to believe that it is the combined effect of friction and rotation that considerably extends the range of applicability of the linear theory. To lend credence to this idea, we have run a real case from the PYREX experiment.

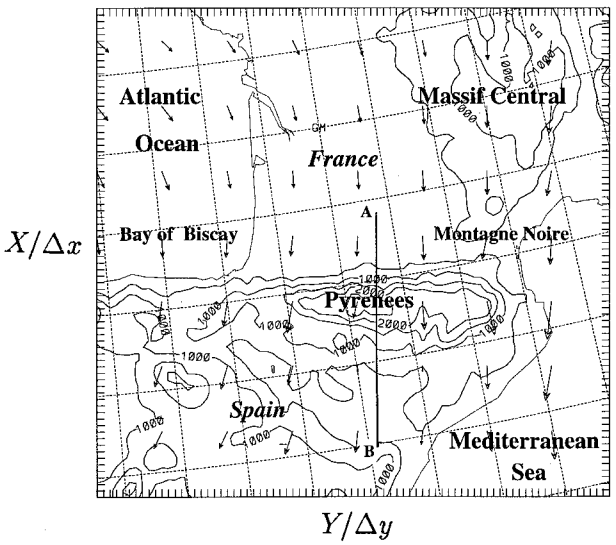

FIG. 15. A map of the Pyrénées, showing the wind field at 3000 m at 0900 UTC 16 November 1990. The topography is indicated with isolines every 500 m. The cross section shown in Fig. 17 is indicated.

6. An example from PYREX

The main purpose of the PYREX campaign was to investigate the atmospheric momentum budget over a major mountain ridge (Bougeault et al. 1993; Bessemoulin et al. 1993). Here, we study a case of northerly flow observed on the 16 November 1990 (intensive observation period 9 or IOP9). This case is illustrated in Fig. 15. Note that the x axis goes from north to south.

The simulations of this case are also carried out with the PERIDOT model, with a 10-km mesh. The model is initialized and forced at the boundaries by the analysis of the 35-km mesh operational PERIDOT, which has been rerun with all available radiosonde data. The topography is defined as $h + \sigma$, where h is the averaged h and σ is the standard deviation of the topography inside a gridbox. The roughness length is set to $\sigma/80$ following Beau (1992).

The simulations of IOP9 have been thorougly validated with all available observations, including the drag that was measured by 14 microbarographs placed on a transect in a central part of the mountain range (I. Beau, personal communication, 1995; Masson and Bougeault 1996; Salvayre 1993).

An important constraint on application of results of simulations of idealized stationary flow to real flows is the nonstationarity of the latter. Here, we have chosen a case where the drag remained relatively constant for about 18 h and transient effects can be expected to be small. However, large and rapid fluctuations were also observed during PYREX and in these cases transient effects may not be negligible.

Determining the nondimensional height Nh/U of the mountain for this real flow is not so obvious. Indeed, vertical variations in N and U pose a major problem because of the various possibilities for averaging. We define a vertical averaging operator as

$$\bar{A} = \frac{1}{Z^*} \int_0^{Z^*} A \, dz. \tag{13}$$

A first approach is to average N and U separately. Another possibility is to average the ratio N/U. These two approaches may result in quite different values, so it is useful to look for theoretical guidance.

The first way to look at the problem is to consider Nh/U as the ratio of the mountain height to the vertical wavelength of hydrostatic mountain waves. Using the WKBJ approach, the local value of the wavelength is proportional to the local value of U/N, and it appears appropriate to average vertically this ratio to measure nonlinear effects. However, when high Nh/U flow approaches the mountain, it enters into a self-induced pressure anomaly. Via such a pressure anomaly, energy may be easily transferred from one layer to another, and it becomes doubtful to make such a computation. Another way is to consider Nh/U as the ratio of the potential and kinetic energy of the low level flow. Here, the measures of the two kinds of energy should be global, and the separate averaging of N and U is favored. The second approach seems more relevant in presence of blocking. Another possibility would be to calculate the nondimensional height for the blocked flow and another nondimensional height for the flow above the blocking. This has been tested by Ólafsson and Bougeault (1996), but they found that the blocked flow and the flow above the blocked flow could not be treated separately.

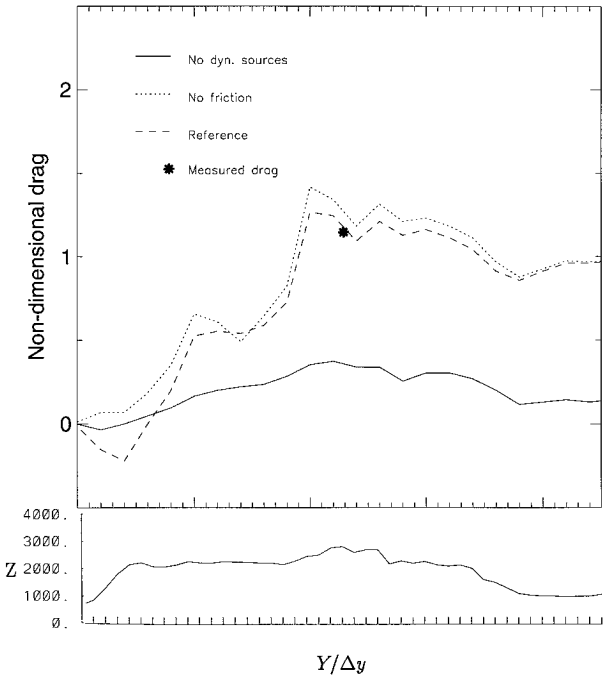

FIG. 16. Cross section along the y axis (transverse to the flow, from east to west), showing the nondimensional drag in 2D sections along the flow for the Pyrénées at 0900 UTC 16 November 1990. The drag is normalized with $\pi\rho_0 NUh^2/4$. The corresponding terrain in a section along the crest of the mountain ridge is given below.

Koffi (1994) calculated the nondimensional mountain height for real flow. He determined U by its value at mountain-top level on a linearized wind profile between 400 m and 6000 m and N is averaged for the same layer. Georgelin (1994) has on the other hand calculated the nondimensional mountain height by averaging U and N in the layer below mountain-top level. Chen and Smith (1987) also calculated the nondimensional height for real flow by averaging N and U in the layer below the mountain-top level. Their main purpose was to study flow splitting, for which the kinetic energy below the mountain-top level may be expected to be of crucial importance.

Our PYREX case clearly features split flow and we choose to average U and N separately. Considering in this case the importance of wind and stability, above as well as below mountain-top level, we choose to integrate up to $Z^* = 2h$, using the simulated wind and stability profile 180 km upstream of the mountain range. This is the layer that we expect to be most strongly affected by the mountains. This gives $\bar{N}h/\bar{U} = 2.4$, which is similar to the value used by Koffi (1994), but smaller than the one of Georgelin (1994).

We have simulated the flow on 16 November 1990 without surface friction and compared this to a reference simulation with realistic values of surface friction. Then, to simulate nonrotating flow we have constructed vertical profiles of stability and wind that correspond to the conditions upstream of the Pyrénées. These profiles are

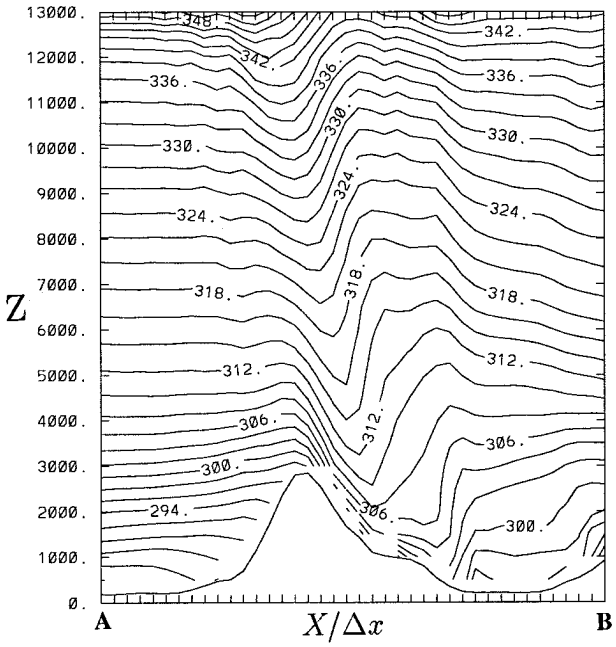

FIG. 17. Potential temperature in a vertical cross section intersecting the central part of the Pyrénées at 0900 UTC 16 November 1990 (see Fig. 15). Here, Z is in meters. The flow is from left to right.

used for initialization and boundary forcing, in a simulation where the flow is not driven by a large-scale pressure gradient, balanced by the Coriolis force.

Figure 16 shows the drag distribution in the y–z plane on 0900 UTC 16 November 1990 for the three simulations. Incidentally, we note the excellent agreement between the observed and simulated values of the drag in the central cross section. This shows that the reference simulation is indeed quite realistic. The main information in Fig. 16 is the large reduction of the drag in the nonrotating case, which confirms the result from the idealized simulations in the same range of Nh/U. Transposing the normalized drag value in the central Pyrenean cross section (from Fig. 16) on the graph in Fig. 4 shows that the reference PYREX simulation, which includes rotation and friction, is closer to the linear value than the two other simulations. Our hypothesis is therefore fully confirmed.

A closer look at Fig. 4 reveals that the normalized drag for the PYREX case is slightly larger than that for the idealized simulations when rotation is present and smaller in the absence of rotation. Figure 17 explains why this is so: the wave amplitude is much greater in the reference PYREX case than for the corresponding simulations of idealized flow with similar value of the nondimensional height. The strong wave activity in the PYREX simulations is probably due to the increase of U and decrease of N with altitude above the mountain-top level (see, e.g., Durran 1986). This emphasizes the importance of vertical structure in real atmospheric flows, not only close to mountain-top level, but also in the upper troposphere. The low drag for the nonrotating flow is presumably also related to the vertical profile of N and U, giving higher values of Nh/U in the lower levels.

It is also visible from Fig. 16 that the rotation more strongly influences the drag in the western part of the ridge (the right of the picture) than in the eastern part. This is in agreement with the asymmetry noted in the idealized simulations. A significant difference, however, is that the distribution of the drag in the y–z plane does not reflect the topography, shown at the bottom of Fig. 16. The high drag values to the west do not correspond to the height of the mountain, while in the east, there is a rapid decrease in the drag, although the topography lowers only a little. The high drag in the west may be explained by accumulation of dense low-level air. Bessemoulin et al. (1993) separated the contributions of five horizontal layers to the total drag, measured in the microbarograph section described previously. They found the contribution of each layer to be proportional to the volume of the mountain elements at the height of the layer. In other words, the lowest levels contributed by far the greatest part of the total drag. This may not necessarily be so if there were only lower topography present, but the high drag in the west indicates that it might be so. We should remember that the Pyrénées are not an isolated ridge, and the surrounding mountains probably explain much of the above differences with the idealized cases. To the west, the Pyrénées are continued by the Cantabric chain, which effectively prevents the low-level flow to find its way on the western flank of the chain. On the contrary, on the eastern side, the Massif Central and the Montagne Noire are separated from the chain by an open channel, which forces a strong westerly flow. This wind increases farther east where it is known as the violent Tramontana wind. In connection to the westerly wind, the accumulation of low-level dense air is reduced rapidly east of the center plane. This affects directly the part of the drag that is due to low-level density differences. It may also be explained by referring to the Coriolis term in Eq. (11) or simply through converson of pressure to kinetic energy.

Another difference from the idealized case is that surface friction reduces the drag, instead of increasing it. We recall that the pressure distributions for EX27P and EX27PF are quite different and that the three-dimensional flow in the lee is responsible for the flat-bottom lee low in EX27PF. In the lee of the Pyrénées, there is not a flat plane, but a wide valley, leading the flow southeast to the Mediterranean Sea. Therefore, it is not surprising that we find surface friction to act to reduce the drag for this real flow simulation, which is opposite to the results of the idealized simulations. Furthermore, the drag reduction by surface friction in the PYREX case may be related to the wave activity being greater than in the idealized flows. This wave activity is a characteristic of the high-drag regime, where surface

friction reduces the drag. Elkhalfi and Richard (1993) found by simulating two-dimensional flow without rotation from another PYREX case that introduction of surface friction gave much greater reduction in the drag than our case. This is presumably also due to the three-dimensionality, being able to account for the effects of flow splitting, but surface friction may also be expected to act differently in the absence of a large-scale pressure gradient and the Coriolis force (Bougeault 1994).

7. Summary and discussion

In this paper we have found some important differences between orographic flows driven by a large-scale pressure gradient, balanced by the Coriolis force, and flows forced only by the boundary conditions on a nonrotating plane. First, the reduction of the pressure drag by rotation predicted by the linear theory for very small values of Nh/U actually remains qualitatively valid for higher values: it extends into the high drag state ($Nh/U \simeq 1.4$). On the other hand, for still higher values of Nh/U, that is, in the presence of blocking, the effect of rotation is opposite: the drag is increased. This contrasting behavior may be explained by the process of geostrophic adjustment, that acts to first order as a relaxation toward the geostrophic wind. In the linear and high drag regimes, the flow is dominated by the velocity increase close to the mountain crest, and the rotation will tend to mitigate this velocity increase, thereby resulting in a damping effect, and a reduction of the drag. In the split flow regime, the flow is dominated by upstream blocking, and rotation will tend to accelerate the flow in the blocking, thereby generating an increase of the drag. In the latter case, the drag is mainly due to the accumulation of dense air upstream of the mountain.

The effect of surface friction has also been investigated in the rotating case. The main result here is a *complete suppression of wave breaking,* related to an important decrease of the drag in the high drag regime. In the split flow regime, the effect of surface friction is a modest increase in the pressure drag. This is due to a flat-bottom low in the wake, produced by increased subsidence of warm air. Surface friction also flattens and decreases the upstream pressure anomaly.

The overall combined effect of rotation and friction on orographic flows in the nonlinear flow regimes is to constrain the drag to remain closer to the linear prediction. This is valid for Rossby number 2.5, which is a typical value for midlatitude mountain ranges of the size of the Pyrénées. The two processes generally act in the same direction, but the main contributor is friction in the high drag regime and rotation in the split flow regime. This result may explain why the drag observations of Bessemoulin et al. (1993) during PYREX could be so well predicted by the most simple 2D, nonrotating, linear theory.

We have also studied the asymmetry of the drag distribution in the direction transverse to the flow. The drag appears to be generally higher on the right side of the mountain than on the left side (facing downstream). The drag asymmetry is in agreement with Smith's (1979) 2D theory on the effects of the Coriolis force, when this theory is applied locally on each side of the central section of the flow. This asymmetry can also be related to asymmetric flow in the wake, favoring advection of low-level dense air on the left side. The increased drag asymmetry at the introduction of surface friction is due to reduction of the wave activity.

Some of our simulations allow us to explore the sensitivity of these results to the mountain aspect ratio. In general, circular mountains give similar results as a mountain ridge with aspect ratio 5, but with smaller intensity. For split flow ($Nh/U = 2.7$), a circular mountain has about half the drag of the mountain ridge in the centerplane of the flow, and the total drag of the mountain ridge is more than eight times the drag of the circular mountain. The corresponding factor given by Phillips (1984) linear theory is only 6.2. This indicates that nonlinear effects become increasingly important for increasing mountain aspect ratio. Moreover, the waves over the mountain ridge are more pronounced than over the circular mountain, and there is more accumulation of dense air upstream of the mountain ridge and descent of warm air in the wake. The effect of rotation on the drag increases with the aspect ratio. This indicates an increasing importance of the low-level density anomalies in the total drag.

The study of one intensive observation period of PYREX has confirmed the main results of our idealized experiments: there are large differences in the drag produced in simulations with and without the Coriolis force. Moreover, surface friction suppresses all wave breaking, and does not change significantly the drag for this particular flow regime. The minor differences between the behavior of the idealized experiments and the more realistic PYREX case could be explained by the existence of vertical variations of N and U, favoring strong wave activity, and surrounding mountains that change the spatial distribution of the drag. We therefore consider that our idealized simulations are relevant to interpret the behavior of more realistic orographic flows, provided that the synoptic flow evolves slowly.

The important impact of rotation and friction evidenced in the present paper calls for a critical review of previous results on orographic flows where these processes are omitted. In the real atmosphere, some ageostrophic flows, such as gap winds, may be expected to behave in a different manner than geostrophic flows, as they meet an obstacle. For a given nondimensional height, an ageostrophic flow may be blocked, while a geostrophic flow is not. In a blocked state, ageostrophic flow may give less drag than geostrophic flow. It should be kept in mind that the celebrated regime diagram of Smith (1989a) is valid only for nonrotating flows. From the present results, we may hypothesize that the curve indicating the transition to flow splitting on this diagram

should be moved upward to take into account the effect of rotation. This is, in fact, in the opposite direction to what could be expected due to the nonlinear effects of wave breaking (Smith and Grønås 1993). Another interesting speculation stems from our observation that friction suppresses wave breaking in the idealized simulations. This suggests that a favorable vertical structure may be a necessary condition for wave breaking in the real atmosphere, regardless of the value of Nh/U.

An additional point that has not been discussed here is the effect of surface friction on the morphology of the flow. In the free-slip flow, flow splitting is easily identified by stagnation on the windward slope of the mountain and reversed flow in an upstream blocking region. When surface friction is introduced, no such stagnation is observed and the flow is not reversed upstream of the mountain. Yet, a large part of the flow is diverted to each side of the mountain, and the low-level flow ascends even less than in a flow with the same Nh/U but no surface friction. We expect this absence of surface stagnation to relate to better mixing of horizontal momentum at the presence of surface friction, but wind turning in the Ekman layer may also be important. The kinematic and dynamic aspects of flow splitting will be the subject of a further study.

Acknowledgments. The PYREX experiment was made possible by the participation of a large number of institutes from France, Spain, and Germany. It was funded by *Météo-France*, the *Instituto National de Meteorologia* (Spain), the *Institut National des Sciences de l'Univers* (ARAT, PAMOS, and PAMOY programs), the *Centre National d'Etudes Spatiales*, *Electricité de France*, *Région Midi-Pyrénées*, and *the Deutsche Forschungsanstalt für Luft und Raumfahrt*. We would like to express our deep appreciation to the many colleagues who have participated in the success of the experiment through enormous personal commitment. Haraldur Ólafsson was supported by the Institute of Meteorological Research, Iceland (RV), and the Icelandic Research Council (RANNÍS).

REFERENCES

Beau, I., 1992: Evaluation des paramétrisations de l'effet orographique sous maille dans les modèles de circulation générale à l'aide de PERIDOT 10km. Tech. Rep., Ecole Nationale de la Météorologie, Toulouse, France, 153 pp. [Available from CNRM, 42, Av. Coriolis, 31057 Toulouse, France.]

Bessemoulin, P., P. Bougeault, A. Genoves, A. J. Clar, and D. Puech, 1993: Mountain pressure drag during PYREX. *Beitr. Phys. Atmos.*, **66,** 305–325.

Bougeault, P., 1994: Are 2D simulations a good approximation of orographic flows? An example from PYREX. Preprints, *Sixth Conf. on Mesoscale Processes*, Portland, OR, Amer. Meteor. Soc., 467–470.

——, and P. Lacarrère, 1989: Parameterization of orography-induced turbulence in a meso-beta-scale model. *Mon. Wea. Rev.*, **117,** 1872–1890.

——, B. Bret, P. Lacarrère, and J. Noilhan, 1991: An experiment with an advanced surface parameterization in a mesobeta-scale model. Part II: The 16 June simulation. *Mon. Wea. Rev.*, **119,** 2374–2392.

——, and Coauthors, 1993: The atmospheric momentum budget over a major mountain range: First results of the PYREX field program. *Ann. Geophys.*, **11,** 395–418.

Chen, W.-D., and R. B. Smith, 1987: Blocking and deflection of airflow by the Alps. *Mon. Wea. Rev.*, **115,** 2578–2597.

Clark, T. L., and W. R. Peltier, 1977: On the evolution and stability of finite amplitude mountain waves. *J. Atmos. Sci.*, **34,** 1715–1730.

——, and ——, 1984: Critical level reflection and the resonant growth of nonlinear mountain waves. *J. Atmos. Sci.*, **41,** 1715–1730.

Durran, D., 1986: Another look at downslope windstorms. Part I: On the development of analogues to supercritical flow in an infinitely deep, continuously stratified fluid. *J. Atmos. Sci.*, **43,** 2527–2543.

Eliassen, A., 1980: Balanced motion of stratified rotating fluid induced by bottom topography. *Tellus*, **32,** 537–547.

——, and E. Palm, 1960: On the transfert of energy in stationary mountain waves. *Geophys. Norv.*, **22,** 1–23.

Elkhalfi, A., and E. Richard, 1993: Simulations bidimensionelles d'ondes de montagne observées lors de l'expérience PYREX. *Atelier de la Modélisation de l'Atmosphère*, Centre National de Recherches Météorologiques, 151–164.

Georgelin, M., 1994: Étude numerique de l'ecoulement atmospherique au voisinage des Pyrénées. Ph.D. thesis, Université Paul Sabatier, Toulouse, France, 158 pp.

——, E. Richard, M. Petitdidier, and A. Druilhet, 1994: Impact of subgrid scale orography parameterization on the simulation of orographic flows. *Mon. Wea. Rev.*, **122,** 1509–1522.

Gill, A. E., 1982: *Atmosphere–Ocean Dynamics.* Int. Geophys. Ser., Vol. 30, Academic Press, 622 pp.

Imbard, M., A. Joly, and R. du Vachat, 1986: Le modèle de prévision numérique PERIDOT: Formulation dynamique et modes de fonctionnement. Tech. Rep. 161, EERM, 70 pp. [Available from CNRM, 42, Av. Coriolis, 31057 Toulouse, France.]

Klemp, J. B., and D. K. Lilly, 1978: Numerical simulation of hydrostatic mountain waves. *J. Atmos. Sci.*, **35,** 78–107.

Koffi, E. N., 1994: Caracterisation experimentale de l'ecoulement atmospherique autour d'un massif montagneux (experience PYREX). Ph.D. thesis, Université Paul Sabatier, Toulouse, France, 213 pp.

Lilly, D. K., 1972: Wave momentum flux—A GARP problem. *Bull. Amer. Meteor. Soc.*, **53,** 17–23.

Masson, V., and P. Bougeault, 1996: Numerical simulations of a low-level wind created by complex orography: A cierzo case study. *Mon. Wea. Rev.*, **124,** 687–700.

Miranda, P. M. A., and I. N. James, 1992: Non-linear three-dimensional effects on gravity-wave drag: Splitting flow and breaking waves. *Quart. J. Roy. Meteor. Soc.*, **118,** 1057–1081.

Ólafsson, H., 1996: Atlas des écoulements hydrostatiques autour d'un relief idéalisé. Tech. Rep. 42, Centre National de Recherches Météorologiques, Météo-France, 86 pp. [Available with an English abstract from CNRM, 42, Av. Coriolis, 31057 Toulouse, France.]

——, and P. Bougeault, 1996: Nonlinear flow past an elliptic mountain ridge. *J. Atmos. Sci.*, **53,** 2465–2489.

Peltier, W. R., and T. L. Clark, 1979: The evolution and stability of finite-amplitude mountain waves. Part II: Surface wave drag and severe downslope windstorms. *J. Atmos. Sci.*, **36,** 1498–1529.

——, and ——, 1983: Nonlinear mountain waves in two and three spatial dimensions. *Quart. J. Roy. Meteor. Soc.*, **109,** 527–548.

Phillips, D. S., 1984: Analytical surface pressure and drag for linear hydrostatic flow over three-dimensional elliptical mountains. *J. Atmos. Sci.*, **41,** 1073–1084.

Pierrehumbert, R. T., and B. Wyman, 1985: Upstream effects of mesoscale mountains. *J. Atmos. Sci.*, **42,** 977–1003.

Richard, E., P. Mascart, and E. C. Nickerson, 1989: The role of surface friction in downslope windstorms. *J. Appl. Meteor.*, **28,** 241–251.

Salvayre, L., 1993: Comparison des resultats du modèle PERIDOT

et des observations faites pendant l'experience PYREX. Tech. Rep., Université Paul Sabatier Toulouse III, France, 60 pp. [Available from CNRM, 42, Av. Coriolis, Toulouse, France.]

Schär, C., and R. B. Smith, 1993: Shallow-water flow past isolated topography. Part II: Transition to vortex shedding. *J. Atmos. Sci.,* **50,** 1401–1412.

Smith, R., 1979: The influence of the earth's rotation on mountain wave drag. *J. Atmos. Sci.,* **36,** 177–180.

——, 1980: Linear theory of stratified flow past an isolated mountain. *Tellus,* **32,** 348–364.

——, 1989a: Hydrostatic airflow over mountains. *Advances in Geophysics,* Vol. 31, Academic Press, 59–81.

——, 1989b: Mountain induced stagnation points in hydrostatic flows. *Tellus,* **41A,** 270–274.

——, and S. Grønås, 1993: Stagnation points and bifurcation in 3-D mountain airflow. *Tellus,* **45A,** 28–43.

Smolarkiewicz, P., and R. Rotunno, 1989: Low Froude number flow past three-dimensional obstacles. Part I: Baroclinically generated lee vortices. *J. Atmos. Sci.,* **46,** 1154–1164.

——, and ——, 1990: Low Froude number flow past three-dimensional obstacles. Part II: Upwind flow reversal zone. *J. Atmos. Sci.,* **47,** 1498–1511.

Stein, J., 1992a: Contribution à l'étude des régimes hydrostatiques d'écoulements orographiques. Ph.D. thesis, Université Paul Sabatier, Toulouse, France, 243 pp. [Available from CNRM, 42, Av. Coriolis, Toulouse, France.]

——, 1992b: Investigation of the regime diagram of hydrostatic flow over a mountain with a primitive equations model. Part I: Two dimensional flows. *Mon. Wea. Rev.,* **120,** 2962–2976.

Sun, W.-Y., and J.-D. Chern, 1994: Numerical experiments of vortices in the wake of large idealized mountains. *J. Atmos. Sci.,* **51,** 191–209.

Thorsteinsson, S., 1988: Finite amplitude stratified air flow past isolated mountains on an f-plane. *Tellus,* **40A,** 220–236.

Wahr, J. M., and A. H. Oort, 1984: Friction and mountain torque estimates from global atmospheric data. *J. Atmos. Sci.,* **41,** 190–204.